Research Square

Preprints are preliminary reports that have not undergone peer review.
They should not be considered conclusive, used to inform clinical practice,
or referenced by the media as validated information.

Identification of Gallagyldilacton as a Mutation-Biased EGFR Inhibitor from Punica granatum Peel via Integrative Computational Analysis

Doğacan Jeremy Edens
Adana Alparslan Türkeş Science and Technology University
Özgür Cem Erkin
ocemerkin@atu.edu.tr

Adana Alparslan Türkeş Science and Technology University

Article

Keywords: Non-small cell lung cancer, epidermal growth factor receptor mutations, network pharmacology, molecular docking, Punica granatum.

Posted Date: March 10th, 2026

DOI: https://doi.org/10.21203/rs.3.rs-8583101/v1

License: This work is licensed under a Creative Commons Attribution 4.0 International License. Read Full License

Additional Declarations: No competing interests reported.

Abstract

Non-small cell lung cancer (NSCLC) accounts for the majority of lung cancer cases worldwide and remains a leading cause of cancer-related mortality. Aberrant activation of the epidermal growth factor receptor (EGFR), driven by overexpression or mutation, represents a central oncogenic mechanism in NSCLC and a primary target of tyrosine kinase inhibitors (TKIs). Despite substantial clinical success, the emergence of resistance-conferring EGFR mutations continues to limit the long-term efficacy of existing therapies. In this study, we employed an integrative *in silico* framework combining network pharmacology, molecular docking, molecular dynamics simulations, and MM-PBSA analyses to investigate the therapeutic potential of phytochemicals derived from *Punica granatum* peel against NSCLC-associated molecular targets. Network analysis identified EGFR, AKT1, and matrix metalloproteinases (MMPs) as key nodes within NSCLC-related signaling pathways. Among the screened compounds, gallagyldilacton and naringenin emerged as prominent candidates with distinct target interaction profiles. Gallagyldilacton exhibited computationally stable and energetically favorable binding to multiple mutant EGFR variants, including T790M and L858R, while displaying comparatively weaker affinity toward wild-type EGFR, consistent with a mutation-biased inhibitory profile. In contrast, naringenin demonstrated preferential interactions with AKT1 and select MMPs, consistent with potential modulation of proliferative and metastatic signaling pathways. Comparative analyses with approved TKIs revealed that gallagyldilacton achieves binding stability and interaction patterns comparable to established inhibitors for specific EGFR mutants. Collectively, these findings support the potential of *Punica granatum* peel phytochemicals as sources of selective, multitarget modulators in NSCLC and highlight gallagyldilacton as a compound exhibiting mutation-biased EGFR interactions and a candidate for further experimental investigation.

INTRODUCTION

Lung cancer remains a prime contributor to the global cancer burden[1]. With non-small cell carcinoma (NSCLC) and small-cell carcinoma (SCLC) accounting for approximately 85% and 15% of lung cancer cases, respectively [2], the disproportionate research focus on the former is unsurprising. While relatively recent efforts to curb population-level risk behaviors—most notably cigarette smoking—have met with success in many Western nations, governments of emerging economies such as Turkey, India, and China have yet to incite comparable nationwide cessation trends. Consequently, the high prevalence of lung cancer, particularly NSCLC, persists in these regions, effectively prolonging the global impact of the disease. Contemporary treatment modalities emphasize early detection, followed by patient enrollment into chemotherapy or invasive surgical interventions, often coupled with adjuvant chemotherapy. In particular, NSCLC chemotherapy has largely centered on inhibition of the EGFR, which exhibits the highest frequency of overexpression and/or mutation among NSCLC patients, followed by aberrant signaling involving the Kirsten rat sarcoma viral oncogene (KRAS) [3].

Over the years, efforts to therapeutically target EGFR—particularly through tyrosine kinase inhibitors (TKIs)—have yielded varying degrees of success. A primary limitation of clinically deployed TKIs, such as osimertinib, as well as earlier agents including erlotinib and gefitinib, is the inevitable development of drug resistance in NSCLC, progressively diminishing therapeutic efficacy over successive treatment cycles. Both pre-existing mutations within the EGFR-encoding gene and those acquired during therapeutic intervention constitute major obstacles to sustained clinical success. Accordingly, a primary objective in the development of novel TKIs is to achieve effective inhibition across multiple mutant forms of the target. For instance, the most prevalent EGFR mutant forms arise from single-point substitutions at residues T790 and L858, in which threonine and leucine are replaced by methionine (~ 50% of patients) and arginine (~ 41% of patients), respectively [4]. The therapeutic landscape of NSCLC chemotherapy includes EGFR-TKIs such as erlotinib and gefitinib, as well as their successors, including afatinib, dacomitinib, and osimertinib. With the overarching goal of improving disease control, these agents were developed to counteract distinct classes of

EGFR mutations. For example, dacomitinib, which was designed to improve upon the efficacy of first-generation agents, demonstrated enhanced activity against less common EGFR mutations, including G719X, L747X, and S768I. Emerging therapeutic strategies—including next-generation TKIs, antibody–drug conjugates, novel immunotherapeutic approaches, and targeted protein degraders—have demonstrated considerable promise in patients with progressive EGFR-mutant NSCLC following EGFR-TKI treatment, despite the persistent challenge of acquired resistance [5]. The accelerating pace of such drug development can be attributed to the increasing sophistication of contemporary methodologies alongside the implementation of novel approaches. In recent years, network pharmacology and computational drug design have played pivotal roles in advancing oncological research. Furthermore, incorporation of complementary analytical strategies—such as molecular dynamics simulations, MM-GB/PBSA calculations, quantitative structure–activity relationship (QSAR) modeling, and ADME profiling—has markedly enhanced the precision of drug discovery and design.

Researchers have shown increasing interest in applying these techniques to natural compounds, particularly plant-derived flavonoids and polyphenols. Consequently, a paradigm has emerged centered on the systematic exploration of ethnopharmacologically relevant botanical sources, many of which have been traditionally utilized by communities maintaining long-standing medicinal practices. Such plants have been used for millennia within these populations, with knowledge of their beneficial effects transmitted across generations through oral tradition. Industrialization and urbanization have inevitably contributed to a global shift away from reliance on such traditional knowledge systems. Nevertheless, the wide array of ameliorative properties attributed to these plants has increasingly been substantiated, and their underlying mechanisms of action have begun to be elucidated. These properties include anti-inflammatory, antidiabetic, antibacterial, and anticancer activities [6].

Among such plants is *Punica granatum* L. (*P. granatum*), commonly known as pomegranate. *P. granatum* belongs to the *Lythraceae* family and is generally believed to originate from the mountainous regions of Iran and Iraq, although aspects of its taxonomy and geographic origin remain debated [6]. The pomegranate plant produces a diverse array of bioactive compounds, primarily flavonoids and anthocyanins. While all parts of the plant have piqued the interest of researchers, the most commonly investigated is the fruit itself. The fruit, being composed of peel, arils, and seeds at a ratio of 5:4:1, is where these compounds of interest are the most abundant. A variety of conditions, such as neurodegenerative diseases, cancer, and diabetes, have been reported to be ameliorated by phytochemicals such as proanthocyanidins, phenolics, ellagitannins, and complex polysaccharides from the fruit [7, 8]. On the other hand, the peel of the fruit which generally tend to be regarded as a waste product, is proven to be a good source of bioactive compounds such as polyphenols, anthocyanins, flavonoids and tannins. Although the content and composition of compounds found in the peel can differ vastly between the varieties, gallo tannins, ellagic acid, punicalins, punicalagins and gallic acid were found to be the most abundant phytochemicals. In addition, owing to differences in *P. granatum* varieties, the content and composition of other biologically active compounds such as catechin, quercetin, kaempferol, chlorogenic acid and naringenin can also be found in varying amounts in the peel [9]. For instance, reports of the concentration of ellagic acid found in *P. granatum* differ greatly between the varieties, Zivzik and Manfalouty [9, 10]. Furthermore, the composition of compounds found within the peel seems to vary heavily within specimens of the same cultivar based on the stage of maturation at which the fruit is harvested. Regardless, there is concrete evidence of a varying but constant presence of compounds that exhibit anticancer properties in *P. granatum* [9–16]. Compounds such as ellagic acid, naringenin, punicalagin, and pedunculagin have been reported to have efficacy on various cancer cell lines ranging from MCF-7 to A549 to HCT-116 *in vitro* [17–20]. Although the molecular composition of the peel varies, the anticancer activity remains consistent, suggesting that this effect is not necessarily due to the activities of multiple compounds but rather to stronger inhibitory activity that results from the compounds' synergy. Lastly, the fact that the peel of the fruit is where most of the beneficial compounds are concentrated has massive implications, as industries

interested in the fruit itself generally process the arils' contents and dispose pomegranate marcs. The theoretical utilization of a waste product produced at such a massive scale as a means of introducing novel drugs for a variety of ailments holds within it the promise of an eco-friendly contribution to medicine, not to mention the profitability of such an endeavor. Many studies have assessed the *in vitro* cancer cell viability of *P. granatum* extracts or certain compounds within different parts of the fruit as potential treatment for NSCLC, and thus have created progenitor research which could potentially catalyze the development of derivative drugs [21–23]. Punicalagin, punicafolin, and other phytochemicals such as genistein derived from *P. granatum*, have shown promise as multitarget therapy agents for a variety of malignancies, including breast cancer, hepatocellular carcinoma, and non-small cell lung cancer. Key overlapping molecular targets that regularly identified by network-pharmacology analyses are AKT1, STAT3, CASP3, SRC, IL6, and NOS3, which are involved in important pathways such PI3K–AKT, JAK–STAT, AMPK, HIF-1α, and mTOR. Despite expression-level fluctuations, strong and stable binding interactions, such as those between genistein and AKT1, punicalagin and SRC/AKT1/CASP3, and punicafolin and STAT3, were supported by molecular dynamics simulations. These computational predictions were further validated by complementary actual results, such as apoptosis induction, G0/G1 arrest, ROS generation in lung cancer cells, and decreased expression of oncogenic targets in HCC. Additionally, pomegranate peel chemicals show dual potential by binding SARS-CoV-2 proteases (Mpro, PLpro), indicating antiviral importance. Together, these investigations show the therapeutic adaptability of plant-derived polyphenols as modulators of networks that drive inflammation and cancer, emphasizing network pharmacology and integrated validation approaches as potent pipelines for mechanistic discovery [24–27]. Therefore, by using an integrative network pharmacological method, we investigated the potential inhibitory effects of phytochemicals from *P. granatum* peel on encoded proteins of upregulated genes in NSCLC. Among other peel phytochemicals, gallagyldilacton promises a pan-EGFR inhibitory potential which might represent a way of powerful intervention in the treatment of EGFR mutant NSCLCs.

RESULTS

Compound–Target Network and Enrichment Analyses

The compound–target network (Fig. 1b) comprised 449 nodes and 6,842 edges, indicating extensive compound–protein associations. On average, each curated *P. granatum* compound interacted with approximately 270 predicted targets, and the overall network exhibited a mean node degree of 16.10. Hub proteins with the highest degrees included ABO (P16442), ADAM17 (P78536), and THRB (P10828), with degree values of 47, 35, and 32, respectively.

The compiled list of upregulated differentially expressed genes (DEGs) from NSCLC literature consisted of 832 unique targets (**Supplementary Table S1**). Intersection of the DEG list with PharmMapper [28]-predicted targets yielded 58 overlapping proteins (Fig. 1a). These overlapping targets were subsequently used to construct a protein–protein interaction (PPI) network (Fig. 1c), which contained 82 nodes and 1,204 edges. Among compound nodes, cyanidin and delphinidin exhibited the highest degrees (50 each), while gallic acid showed the lowest (degree = 36). Target proteins displayed an average degree of 22.95, with EGFR representing a highly connected node (degree = 39) and SPARC exhibiting lower connectivity (degree = 3), indicating differences in network connectivity between these proteins.

Functional enrichment analysis integrated Gene Ontology (GO), KEGG [29], WikiPathways, Reactome gene sets, and canonical pathways (Fig. 2a). GO and KEGG analyses identified significant enrichment in carboxylic acid metabolic processes (GO:0019752, log p = − 15.61), hormonal response (GO:0009725, log p = − 15.58), and collagen catabolic processes (GO:0030574, log p = − 11.86) (Fig. 2b). Nuclear receptor signaling (R-HSA-9006931, log p = − 13.89) was also prominently represented, alongside pathways related to extracellular matrix disassembly, proteoglycans in cancer, and regulation of cell migration.

Within the carboxylic acid metabolic process cluster, monocarboxylic acid metabolism (GO:0032787) emerged as the most significant subnode (log p = − 14.73). Transcription factor enrichment analysis identified SP1 as the dominant regulator (log p = − 16), associated with a large subset of overlapping targets including CBS, EGFR, ESR1, MIF, MMP9, MMP12, OAT, and PLAU (Fig. 2c). Protein network analysis further defined a set of core targets (Fig. 3a). These representative core targets, except PLAU, were selected for subsequent molecular docking and simulation analyses.

Molecular Docking

A total of 386 ligand–protein docking simulations were performed, of which 374 produced valid docking poses. Twelve docking attempts failed due to positive binding energy values (> 0 kcal/mol). Twelve ligand–protein complexes exhibited estimated inhibition constants in the nanomolar range, with the majority involving MMP9 and MMP13. A summary of docking energies is provided in Fig. 3b, and calculated inhibition constants are listed in **Supplementary Table S5** online.

When assessed at the protein level, approximately one-third of the core target proteins were inhibited by at least one ligand with nanomolar-range affinity. Representative binding modes for the top-ranked complexes are shown in Fig. 4, and interaction profiles before and after molecular dynamics (MD) simulations are summarized in Table 1. Docking results were used to rank ligand–protein complexes based on predicted binding affinity, and MD simulations were subsequently performed to evaluate the stability of selected interactions.

Table 1 Binding interactions of selected compounds with target proteins before and after MD simulations. a) Ligand-protein interactions of chosen complexes prior to MD simulation. b) Post-MD simulation complex interactions.

Table 1 a

	[n] indicates repetition			Aromatic Interactions	
Target	**Ligand**	**Hydrophobic Interactions**	**Hydrogen Bonds**	**π-stackingπ-cation**	**Other Interactions**
Chlorogenic Acid	MMP13	L185, L218, V219*[2]*	L185, A186*[2]*, H222*[2]*		Salt bridge:H222
		H222, L239, Y244	E223, F241, I243*[2]*		
			T245*[2]*		
Naringenin		L185*[2]*, V219, H222	S182, G183, L185	H222	
			A186, Y214*[2]*, Q223		
			Y244		
	MMP12	V235, F237, Y240*[2]*	L181, A182*[2]*, T215	H218	Salt bridge:H218, H228
			P232, T239		
	AKT1	W80, T82, I84	N54, Q79*[3]*, Q203	W80	
		K268, D292	T211, K268, Y272		
	OAT	Y85, E230, E235	Y85*[2]*, R180*[2]*, I232	F177K292	Salt bridge:K292
		I265, Q266	Q266, T267		
Gallagyldilacton	EGFR	L718*[2]*, V726	L718, K745, R776		Salt bridge:K745
			T790, M793*[2]*, C797		
			T854, D855		
	MMP3	H166, Y168	Y155*[3]*, H166, A167*[2]*	Y155H211	Salt bridge:H166, H205
			A169, N175, E202*[3]*		Metal complex: Zn + 2
	MMP7	Y172, T180, L181 Y240	T180*[2]*, A182, A184*[2]* E219, Y240	H183	Salt bridge:H218, H222, H228 Metal complex: Zn + 2
Epicatechin	MMP9	L188, L222, V223	H226, E227*[4]*, A242		
		H226, Y248*[2]*, R249	L243, R249*[2]*		
Kaempferol		L188, V223, H226	E227*[2]*, A242, Y245	H226	

	[n] indicates repetition			Aromatic Interactions	
		Y245, Y248, R249	R249*[2]*		
Luteolin		L188, L222, H226	E227*[4]*, A242, R249*[3]*		
		Y248, R249, T251	T251		
Pelargonidin		L188, L222, V223*[2]*	E227*[2]*, A242, R249	H226	
		H226, Y248*[2]*, R249			
Table 1b					
				Aromatic Interactions	
Target	**Ligand**	**Hydrophobic Interactions**	**Hydrogen Bonds**	**π-stackingπ-cation**	**Other Interactions**
Chlorogenic Acid	MMP13	L185	L185, A186*[3]*, F241		
			T245*[3]*, H251, M253		Salt bridge:H222
Naringenin		L185, V219, H222*[2]*	L185, A186*[2]*		
		P242			
	MMP12	L214*[2]*, H218, V235	L181, A182*[2]*, H218		Salt bridge:H218
		P238, T239, V243			
	AKT1	W80, L210, L264	H207, V271, Y272		
	OAT	W178, I265*[2]*, Q266	G51, Y55, L58	Y55	Salt bridge:K292
			G142, V143, E230		
Gallagyldilacton	EGFR	L718*[2]*, L844	M793, C797, T854*[2]*		
			D855		
	MMP3		D158, P160*[2]*, A167	F86	Salt bridge: H166*[2]*, H211
			A169		
	MMP7	Y172*[2]*	Y172, D175*[2]*	Y172*[2]*	
Epicatechin	MMP9	Y248, R249	C99	H226	

[n] indicates repetition			Aromatic Interactions
Kaempferol	L222, Y248, T251	E241	
Luteolin	L188, V223, H226	A189*[2]*, V223, R249	H226
	Y238		
Pelargonidin	L222, L243*[2]*, R249	E241, Y245, R249	Y248
	T251	T247	

Molecular Dynamics Simulations and MM-PBSA Calculations

MD simulations identified several ligand–protein complexes that remained stable over 100 ns trajectories, including EGFR–gallagyldilacton, MMP9–luteolin, MMP12–naringenin, MMP13–naringenin, and MMP13–chlorogenic acid. MM-PBSA analysis (Table 2) identified chlorogenic acid–MMP13 complex, with the lowest binding free energy of ΔG_bind = − 34.47 ± 4.34 kcal/mol. RMSD analysis supported the stability of this interaction (Fig. 5a).

Table 2 Binding interactions of chosen TKIs and gallagyldilacton with variant EGFR protein before and after MD simulations. **a)** Table of interactions with EGFR variants in chosen TKIs along with gallagyldilacton prior to simulation **b)** Post-simulation interactions with EGFR variants seen in TKIs and gallagyldilacton.

Table 2 a

	[n] indicates repetition			Aromatic Interactions	
Target	**Ligand**	**Hydrophobic Interactions**	**Hydrogen Bonds**	**π-stackingπ-cation**	**Other Interactions**
EGFR*WT*	Afatinib	L718, V726*[2]*, A743	K745, M793, D855*[2]*	F856	
		K745, T790, L858			
	Dacomitinib	V726, A743, K745 M766, T790, L844*[2]*	T790, M793, T854*[2]* D855		
		F856			
	Gefitinib	V726, A743, K745 T790, L844*[2]*	K745, M793, C797		
	Gallagyldilacton	L718*[2]*, V726	L718, K745, R776 T790, M793*[2]*, C797		Salt bridge:K745
			T854, D855		
EGFR*T790M*	Afatinib	L718, V726, K745	K745, E762, D855*[2]*	K745	
		L844			
	Dacomitinib	L718, V726*[2]*, A743 L844*[2]*	K745		Salt bridge:855
	Gefitinib	L718, L792	K745, M793, D855		
	Gallagyldilacton	L718*[2]*, L844	L718, E762*[2]*, M793*[2]*		Salt bridge:K745
			C797, T854, D855		
			F856		
EGFR*L858R*	Afatinib	E758, I759, R858	K745*[2]*, E762, T854		
			D855		
	Dacomitinib	L718, V726*[3]*, A743 K745*[2]*, L788, L844	V726, D855*[2]*		Salt bridge:E762
	Gefitinib	L844	K745, M793, G796		Salt bridge:D855
			C797, D855		
	Gallagyldilacton	F723, V726, A743 L844	S720*[3]*, K745, Q791 M793, T854*[3]*		K745
EGFR*ex19del*	Afatinib	F723, V726, A743 K745, M793, L844*[2]*	A722, F723, G724 T790, T854, D855		
	Dacomitinib	L718, A743, K745	M793		Salt bridge:D855

	[n] indicates repetition			Aromatic Interactions	
		T790, L844, T854			
	Gefitinib	L718, V726, A743	T790, Q791		
		L792, M793			
	Gallagyldilacton	L844	S720, A722, F723	K745	
		E762, Q791*[2]*, M793			
EGFR*ex20ins*	Afatinib	L718, A743, K745	T793, M796, G799		
		L791, T793, M796			
		L847*[2]*			
	Dacomitinib	L718, V726*[2]*, A743	F859		
		E762, T793, L795			
		M796, L847			
	Gefitinib	L718, V726, A743	T793, M796, G799		Halogen bond:L791
		L795, L847	D858		
	Gallagyldilacton	L718*[2]*, R844	K728, M796, D803 R844, D855*[3]*		

Table 2b

				Aromatic Interactions	
Target	**Ligand**	**Hydrophobic Interactions**	**Hydrogen Bonds**	**π-stackingπ-cation**	**Other Interactions**
EGFR*WT*	Afatinib	V726, A743, L777	M793*[2]*, D855*[2]*		D855
		L858			
	Dacomitinib	K745*[2]*, T790	T790*[2]*, M793, D855		
	Gefitinib	L718, V726, A743 K745*[2]*, T790	G721, M793, C797	K745	
	Gallagyldilacton	L718*[2]*, L844	M793, C797, T854*[2]*		
			D855		
EGFR*T790M*	Afatinib	V726, L844	M793, C797		Salt bridge:D800
	Dacomitinib	L718, L844	M793, T854		Salt bridge:855
	Gefitinib	L844	Q791, M793		

	[n] indicates repetition			Aromatic Interactions	
	Gallagyldilacton	L718*[2]*, K745, L844	S720*[2]*, E762*[2]*, M793*[2]*		Salt bridge:K745
			P794, G796, D855		
EGFR*L858R*	Afatinib	I878	R889		
	Dacomitinib	R841, A859	R841*[3]*	R841*[2]*	Salt bridge:D855
	Gefitinib		Q791, D800		Salt bridge:D855
	Gallagyldilacton	L718, F723, A743	T790, C797, T854		
EGFR*ex19del*	Afatinib	R889. Y891	S885		
	Dacomitinib	V726, A743, K745			
		L788, T790, R841			
		L844			
	Gefitinib	L718, V726, L844	M793		Salt bridge:D800
	Gallagyldilacton	V726	S720*[2]*, K745, M793		
		D855			
EGFR*ex20ins*	Afatinib	L718, A743, K745	Q794, M796		
		T793, L795, L847			
	Dacomitinib	V726, I759*[2]*, M766	T793, L861		Salt bridge:D858
		L791, L861			
	Gefitinib	L718, V726, T857	L718		
	Gallagyldilacton	V726	S720*[2]*, K745, M793		
			D855		

Naringenin displayed stable binding to a subset of its targets, while interactions with AKT1 and OAT exhibited gradual loss of stability over the simulation period (Fig. 5b). RMSD and RMSF analyses of MMP9 complexes revealed variable ligand stability; luteolin maintained stable binding, whereas epicatechin showed weaker interaction profiles (Figs. 5c and 5d, **Supplementary Fig. S1**). Consistent RMSF patterns across all MMP9 simulations confirmed the robustness of the comparative analyses, as all simulations were performed using the same protein structure.

Gallagyldilacton–EGFR complexes displayed moderate overall stability (ΔG_bind = − 7.20 ± 4.53 kcal/mol) while maintaining interactions with key ATP-binding site residues, including K745, T790, and L858 (Tables 2 and 3). Subsequent analyses focused on EGFR-containing complexes.

Table 3

MM/PBSA analysis of stable complexes throughout this study. All values represented in the table are in kcal/mol.

			Δ*EMM*	**Δ*Gsol***				
Protein	**Ligand**	Δ*EvdW*	Δ*Eelectrostatic*	Δ*GP B*	Δ*GSA*	Δ*EMM*	Δ*Gsol*	Δ*Gbind*
EGFR	Afatinib	-57.28 ± 3.16	1.44 ± 11.67	33.2 ± 11.09	-4.97 ± 0.18	-55.84 ± 12.08	28.22 ± 11.05	-27.62 ± 5.38
	Dacomitinib	-52.99 ± 3.2	-62.03 ± 9.43	96.08 ± 8.62	-5.71 ± 0.13	-115.02 ± 9.26	90.37 ± 8.61	-24.65 ± 4.84
	Gefitinib	-49.52 ± 3.1	-28.43 ± 15.78	55.18 ± 13.54	-4.95 ± 0.23	-77.95 ± 15.17	50.24 ± 13.55	-27.72 ± 4.9
	Gallagyldilacton	-49.36 ± 2.79	-14.98 ± 6.21	62.06 ± 7.11	-4.92 ± 0.15	-64.34 ± 6.59	57.14 ± 7.05	-7.2 ± 4.53
EGFR*T790M*	Dacomitinib	-41.64 ± 3.32	-112.54 ± 16.9	140.87 ± 19.11	-4.39 ± 0.26	-154.18 ± 17.99	136.48 ± 19.02	-17.7 ± 4.83
	Gallagyldilacton	-43.58 ± 4.7	-45.11 ± 6.28	63.82 ± 5.32	-4.06 ± 0.12	-88.68 ± 7.61	59.77 ± 5.25	-28.92 ± 4.47
EGFR*L858R*	Gefitinib	-50.21 ± 3.36	-81.7 ± 21.75	114.34 ± 19.55	-5.16 ± 0.18	-131.91 ± 21.54	109.18 ± 19.54	-22.73 ± 5.99
	Gallagyldilacton	-43.61 ± 2.75	-23.41 ± 5.79	47.22 ± 6.51	-4.38 ± 0.19	-67.01 ± 6.24	42.84 ± 6.41	-24.17 ± 3.74
EGFR*ex19del*	Dacomitinib	-52.8 ± 3.49	-85.3 ± 13.88	113.78 ± 17.92	-5.44 ± 0.24	-138.11 ± 15.05	108.34 ± 17.81	-29.76 ± 6.4
EGFR*ex20ins*	Afatinib	-54.67 ± 2.87	-107.17 ± 16.86	144.3 ± 18.34	-5.3 ± 0.17	-161.84 ± 16.93	139 ± 18.29	-22.84 ± 5.19
MMP9	Luteolin	-36.87 ± 3.24	-57.51 ± 4.85	74.54 ± 6.42	-3.25 ± 0.07	-94.38 ± 4.47	71.29 ± 6.42	-23.09 ± 6.87
MMP13	Chlorogenic acid	-44.17 ± 3.16	-70.02 ± 5.67	83.53 ± 4.04	-3.98 ± 0.06	-114.02 ± 5.5	79.55 ± 4.03	-34.47 ± 4.34
OAT	Naringenin	-42.68 ± 2.58	-42.2 ± 4.78	79.54 ± 6.92	-4.33 ± 0.08	-84.88 ± 4.31	-75.22 ± 6.91	-9.67 ± 6.02

Gallagyldilacton was compared with established EGFR TKIs (afatinib, dacomitinib, and gefitinib). All TKIs showed stable binding to EGFR^{WT}, with RMSD values ranging from 1.7 to 2.1 Å. Gallagyldilacton showed RMSD and RMSF profiles within the same range, indicating a similar binding mode (Fig. 6a). In simulations involving EGFR^{T790M} and EGFR^{L858R}, gallagyldilacton demonstrated stability comparable to dacomitinib and gefitinib, respectively (Fig. 6b and

6c). Reduced stability was observed for exon deletion mutants ($EGFR^{ex19del}$; Fig. 6d), whereas binding to $EGFR^{ex20ins}$ was comparable to that of reference TKIs (Fig. 6e).

Post-simulation interaction analyses showed that gallagyldilacton frequently formed a greater number of hydrogen bonds with EGFR variants than the reference TKIs, while consistently engaging critical ATP-binding site residues (Tables 2a and 2b). MM-PBSA calculations revealed a mutation-biased binding profile: gallagyldilacton displayed weaker affinity for $EGFR^{WT}$ but substantially stronger binding to $EGFR^{T790M}$ (ΔG_bind = − 28.92 ± 4.47 kcal/mol) and $EGFR^{L858R}$ (ΔG_bind = − 24.17 ± 3.74 kcal/mol) (Table 3). Van der Waals contributions remained consistent across EGFR variants (− 43.58 to − 49.36 kcal/mol), and favorable desolvation energies contributed to the overall binding free energy.

Stable ligand-protein interactions were observed with both metalloproteins and EGFR across the analyzed complexes. In line with network predictions and dynamic stability analyses, gallagyldilacton showed stable binding to EGFR variants, while naringenin exhibited broader interactions involving AKT1, MMP12/13, and OAT.

DISCUSSION

Non-small cell lung cancer (NSCLC) remains a leading cause of cancer-related mortality worldwide, largely due to the high prevalence of oncogenic mutations in the epidermal growth factor receptor (EGFR) and the inevitable development of resistance to targeted therapies [30]. In this study, we employed an integrative network pharmacology and computational modeling framework to investigate the inhibitory potential of phytochemicals derived from *P. granatum* peel against proteins encoded by genes upregulated in NSCLC. Through this approach, gallagyldilacton emerged as a prominent candidate, exhibiting stable and preferential binding to mutant forms of EGFR that are clinically associated with therapeutic resistance.

Network pharmacology analysis was first used to provide a systems-level context for target prioritization. Among the differentially expressed genes and predicted compound targets, EGFR, AKT1, and several matrix metalloproteinases (MMPs) occupied central positions within the protein–protein interaction network. Rather than implying equivalent biological or clinical relevance for all identified nodes, this analysis served to guide subsequent focused investigations. EGFR was prioritized due to its well-established role as a driver of NSCLC progression and its centrality within both oncogenic signaling and current therapeutic strategies.

Docking and molecular dynamics simulations revealed that gallagyldilacton binds stably to clinically relevant EGFR mutants, particularly $EGFR^{T790M}$ and $EGFR^{L858R}$, while displaying comparatively reduced affinity toward wild-type EGFR. This mutation-biased binding profile is notable, as resistance-conferring mutations such as T790M are a major limitation of first- and second-generation EGFR tyrosine kinase inhibitors (TKIs) [31]. To our knowledge, this study provides early computational evidence suggesting that gallagyldilacton may preferentially accommodate structural alterations introduced by common EGFR resistance mutations, supporting its potential as a mutation-focused inhibitory scaffold.

At the structural level, the stability of gallagyldilacton–EGFR mutant complexes appears to arise from a dense and adaptable hydrogen-bonding network, complemented by favorable van der Waals interactions within the altered binding pockets of mutant receptors. Molecular dynamics analyses indicated that these interactions remain stable over extended simulation times, suggesting that gallagyldilacton can tolerate conformational changes associated with EGFR mutations. Rather than relying on a single dominant interaction, the compound's binding mode reflects a distributed interaction profile, which may be advantageous in the context of structurally heterogeneous mutant targets.

In addition to EGFR, other *P. granatum* peel phytochemicals displayed affinity toward secondary targets within the network. Notably, naringenin demonstrated stable interactions with AKT1 and selected MMPs, proteins implicated in tumor survival, invasion, and microenvironment remodeling. These findings suggest the possibility of complementary network-level modulation; however, the present results do not imply standalone therapeutic relevance for these secondary interactions in NSCLC. Instead, they highlight the broader polypharmacological landscape of *P. granatum*–derived compounds, within which EGFR inhibition remains the primary focus of this work.

When positioned against existing EGFR-targeted therapies, gallagyldilacton does not seek to supplant approved TKIs but rather represents a distinct, mutation-biased inhibitory profile. While third-generation TKIs such as osimertinib were designed to overcome T790M-mediated resistance, the emergence of additional resistance mechanisms continues to challenge long-term efficacy [32]. The computational comparability of gallagyldilacton to known TKIs in mutant EGFR systems underscores its relevance as a lead structure for further exploration, without implying clinical readiness or superiority.

Although this study primarily focuses on target engagement and molecular stability, *in silico* ADME profiling was performed to contextualize gallagyldilacton within a translational framework. As shown in **Supplementary Table S6** online, gallagyldilacton displays acceptable physicochemical properties, including moderate solubility, permeability and intestinal absorption. While these predictions do not replace experimental pharmacokinetic evaluation, they support the feasibility of the phytochemicals as optimization-ready scaffolds and complement the observed binding stability and mutation-spanning target engagement.

Several limitations of this study should be acknowledged. All findings are derived from *in silico* analyses, and experimental validation at the biochemical and cellular levels is required to substantiate inhibitory activity. Additionally, as detailed in the Methods section, entropy contributions were excluded from MM-PBSA calculations due to computational constraints, which may affect the absolute estimation of binding free energies. Nevertheless, relative comparisons across similar systems remain informative within this framework. Future work should focus on experimental validation, structural optimization, and evaluation of biological activity in EGFR-mutant NSCLC models.

In conclusion, this study integrates network pharmacology, molecular docking, molecular dynamics simulations, and MM-PBSA calculations to identify gallagyldilacton as a promising, mutation-biased EGFR-focused inhibitor derived from *P. granatum* peel. By emphasizing selectivity toward resistance-associated EGFR mutants and situating these findings within a systems-level context, this work provides a rational computational foundation for the further investigation of plant-derived polyphenols as candidates for overcoming EGFR-driven therapeutic resistance in NSCLC.

METHODS

Data Acquisition and Preparation

To compile a comprehensive list of differentially expressed genes (DEGs), a literature review of studies published between 2018 and 2023 that analyzed DEGs in NSCLC tumor tissue was conducted (**Supplementary Table S1**). For inclusion, upregulated DEGs with a fold change greater than 2 (FC > 2) were considered significant (**Supplementary Table S2**). Phytochemicals derived from *P. granatum* peel that have been reported to exhibit anticancer activity were collected from the literature, yielding a total of 24 compounds relevant to this study (**Supplementary Table S3**). These compounds encompassed multiple chemical classes, including anthocyanins, ellagitannins, flavonoids, hydroxybenzoic acids, and hydroxycinnamic acids. Following compilation, each compound was retrieved from PubChem [33] in MOL2 format, and its geometry was optimized using Avogadro [34]. To guide subsequent analyses, a dataset of potential protein targets was generated for each compound. Accordingly, PharmMapper [28] was employed to

predict and constrain the set of protein targets analyzed in this study. The parameters “Generate Conformers” and “Select Targets Set” were set to “Yes” and “Human Protein Targets Only“ (v2010, 2241), respectively. Both the compiled DEG list and the predicted targets obtained from PharmMapper were converted into UniProtKB identifiers using the Retrieve/ID mapping service provided by UniProt [35].

Network Construction and Enrichment Analyses

Following target identification, a compound–target interaction network was constructed using Cytoscape (v3.10.3) [36]. Compounds exhibiting a degree value greater than one were selected and subsequently used for enrichment analyses. The compiled DEG list was overlapped with the PharmMapper-derived target list using Venny [37]. The overlapping targets were subsequently subjected to STRING analysis within Cytoscape to generate a protein–protein interaction (PPI) network, into which the active compounds were integrated to visualize their associations with the overlapping proteins [38].

Gene Ontology (GO) and KEGG [29] pathway enrichment analyses were performed using Metascape (v3.5.20250101), a web-based platform designed to integrate multiple OMICS datasets into a unified bioinformatics workflow using the overlapping target proteins identified in Cytoscape. Of relevance to this study was Metascape’s ability to perform pathway enrichment across multiple databases and to subsequently cluster enriched term. Protein network analysis was additionally performed using STRING to identify core nodes based on functional interrelatedness and contribution to molecular assemblies [39].

Protein Preparation and Docking

Selected protein structures were retrieved from the Protein Data Bank (PDB) [40] (**Supplementary Table S4**) and prepared using ChimeraX [41]. Nonstandard atoms were removed from the PDB files, while essential metal ions and solvent molecules were retained. AutoDock 4.2.6 [42] was used to add hydrogen atoms, merge nonpolar hydrogens, assign Kollman charges, and define AD4 atom types. Members of the core protein list obtained via Metascape analyses were subjected to docking via AutoDock. Based on prior literature, residues defining ATP-binding sites or allosteric domains were identified, and the average coordinates of these regions were calculated for each target protein. For docking, a cubic grid box with dimensions of 60 × 60 × 60 points and a spacing of 0.5 Å was centered on the calculated coordinate average. This approach ensured that only literature-validated functional sites and domains with inhibitory potential were considered. Map types were set directly; target proteins that necessitate the presence of metal ions such as zinc, had their ions preserved and were mapped in addition to organic material. Docking simulations were performed using the Lamarckian genetic algorithm implemented in AutoDock 4.2. Each docking was executed with 10 GA runs, a population size of 150, a maximum of 2500000 evaluations, in 27000 generations, and rates of gene mutation and crossover at 0.02 and 0.8, respectively. The number of generations for picking the worst individual was set at 10, while the mean and variance of the Cauchy distribution for gene mutation were set at 0.0 and 1.0, respectively. Docking parameters were set to default, and post-docking ligand-protein interactions, such as hydrogen bonds, salt bridges, etc., were assessed using the Protein-Ligand Interaction Profiler (PLIP) [43].

Molecular Dynamics Simulations and MM-PBSA Calculations

Molecular dynamics (MD) simulations were performed using GROMACS version 2024.4 [44], and ligand–protein complexes exhibiting nanomolar-range inhibition constants were selected for further investigation. Given the prevalence of metalloproteins and associated zinc ions, the CHARMM36 force field—equipped with validated metal ion

parameters, including zinc [45]—and a modified TIP3P water model was employed throughout all MD simulations. Ligand topology was obtained via SwissParam, and proteins were prepared via the DockPrep tool in ChimeraX. Energy minimization (EM) was performed using a step size of 0.01 until the maximum force fell below 10 kcal/mol. Both canonical ensemble isothermal volume (NVT) equilibration and isothermal pressure (NPT) equilibration were run for 100 ps at 2 fs intervals. MD simulations were carried out for 100 ns at 2 fs intervals with the temperature set at 300 K. Subsequent RMSD, RMSF, and H-bond analyses of each MD simulation were carried out internally in GROMACS using built-in functions.

Although implicit generalized Born (GB) models are commonly used for protein–ligand free energy calculations, there is consensus that simulations employing the CHARMM36 force field are better suited to Poisson–Boltzmann (PB)-based approaches. Therefore, Gibbs free energy calculations were done using gmx_MMPBSA via the PB model, which is a free energy computation tool based on AmberTools that is capable of a variety of calculations, the most relevant of which involve ligand-protein MM-PB(GB)SA determinations [46]. In our simulations,calculations took into consideration the last 20 ns of stable complexes, i.e., complexes which attained stability at values ≤ 3 Å, at a set temperature and interval of 300 K and 1, respectively.

Calculations were executed based on the following formulae:

$$\Delta G = \Delta H - T\Delta S \quad (1)$$

$$\Delta H = \Delta E_{MM} + \Delta G_{sol} \quad (2)$$

$$\Delta E_{MM} = \Delta E_{vdW} + \Delta E_{electrostatic} \quad (3)$$

$$\Delta G_{sol} = \Delta G_{PB} + \Delta G_{SA} \quad (4)$$

$$\Delta G_{bind} = \Delta G_{complex} - (\Delta G_{receptor} + \Delta G_{ligand}) \quad (5)$$

Amongst the gmx_MMPBSA provided methods of computing, the terms for enthalpy (TΔS) are C2, interaction entropy, normal mode (NMODE), and quasi-harmonic entropy calculations. The former two methods have low computational cost requirements with the drawback of less precise calculations, whereas the latter two methods have substantially high computational demands. Due to the substantial computational demands of quasi-harmonic entropy and NMODE calculations, the entropic term (TΔS) was excluded from MM-PBSA calculations in this study.

Declarations

COMPETING INTERESTS

The authors declare no competing interests

FUNDING

DECLARATION

This work was not supported by any funding resources.

Author Contribution

Ö.C.E. Conceptualization, Project administration, Formal analysis, Resources, Supervision, Writing-Review and Editing;D.J.E. Data Curation, Investigation, Validation, Writing-Original Draft.

Data Availability

The datasets generated during and/or analyzed during the current study are available from the corresponding author on reasonable request.

References

1. Schabath, M. B. & Cote, M. L. Cancer progress and priorities: Lung cancer. *Cancer Epidemiol. Biomarkers Prev.* **28**, 1563–1579 (2019).
2. Rudin, C. M., Brambilla, E., Faivre-Finn, C. & Sage, J. Small-cell lung cancer. *Nat. Rev. Dis. Primers*. **7** (1), 3, 1–20 (2021).
3. Chevallier, M., Borgeaud, M., Addeo, A. & Friedlaender, A. Oncogenic driver mutations in non-small cell lung cancer: Past, present and future. *World J. Clin. Oncol.* **24** (4), 217–237 (2021).
4. Nie, W. et al. Structural analysis of the EGFR TK domain and potential implications for EGFR targeted therapy. *Int. J. Oncol.* **40**, 1763–1769 (2012).
5. Zhou, F. et al. The changing treatment landscape of EGFR-mutant non-small-cell lung cancer. *Nat. Rev. Clin. Can.* **22**, 95–116 (2025).
6. Xu, J. et al. Punicalagin regulates signaling pathways in inflammation-associated chronic diseases. *Antioxidants (Basel)*. **11** (1), 29 (2022).
7. Modaeinama, S., Abasi, M., Abbasi, M. M. & Jahanban-Esfahlan, R. Anti tumoral properties of *Punica granatum* (pomegranate) peel extract on different human cancer cells. *Asian Pac. J. Cancer Prev.* **16**, 5697–5701 (2015).
8. Zeynalova, A. M. & Novruzov, E. N. Origin, taxonomy and systematics of pomegranate. *PROCEEDINGS OF THE INSTITUTE OF BOTANY, ANAS* 37, 21–26 (2017).
9. Singh, J. et al. Pomegranate peel phytochemistry, pharmacological properties, methods of extraction, and its application: a comprehensive review. *ACS Omega*. **8**, 35452–35469 (2023).
10. Panth, N., Manandhar, B. & Paudel, K. R. Anticancer activity of *Punica granatum* (pomegranate): a review. *Phytother. Res.* **31**, 568–578 (2017).
11. Xu, P. et al. Analysis of the Molecular Mechanism of Punicalagin in the Treatment of Alzheimer's Disease by Computer-Aided Drug Research Technology. *ACS Omega*. **7**, 6121–6132 (2022).
12. Karagecili, H., İzol, E., Kirecci, E. & Gulcin, İ. Determination of antioxidant, anti-alzheimer, antidiabetic, antiglaucoma and antimicrobial effects of Zivzik pomegranate (*Punica granatum*)—a chemical profiling by LC-MS/MS. *Life* **13**, 735: 1–27 (2023).
13. Zaki, S. A. et al. Phenolic compounds and antioxidant activities of pomegranate peels. *Int. J. Food Eng.* **1** (2), 73–76 (2015).
14. Zhao, X., Yuan, Z., Fang, Y., Yin, Y. & Feng, L. Characterization and evaluation of major anthocyanins in pomegranate (*Punica granatum* L.) peel of different cultivars and their development phases. *Eur. Food Res. Technol.* **236**, 109–117 (2013).
15. Satomi, H. et al. Carbonic anhydrase inhibitors from the pericarps of *Punica granatum* L. *Biol. Pharm. Bull.* **16**, 787–790 (1993).

16. Elango, S., Balwas, R. & Padma, V. V. Gallic acid isolated from pomegranate peel extract induces reactive oxygen species mediated apoptosis in A549 cell line. *J. Cancer Ther.* **02**, 638–645 (2011).
17. El-Hadary, A. E. & Ramadan, M. F. Phenolic profiles, antihyperglycemic, antihyperlipidemic, and antioxidant properties of pomegranate (*Punica granatum*) peel extract. *J. Food Biochem.* **43** (4), e12803 (2019).
18. Tawfek, A. M. et al. Protective effect of *Punica granatum* peel extract and its alginate-encapsulated nanoparticles against acrylamide-induced neurotoxicity in rats. *Egy J. Pure Appl. Sci. vol.* **62** (1), 1–19 (2024).
19. El-Hamamsy, S. M. A. & El-khamissi, H. A. Z. Phytochemicals, antioxidant activity and identification of phenolic compounds by HPLC of pomegranate (*Punica granatum* L.) peel extracts. *J. Agricultural Chem. Biotechnol.* **11**, 79–84 (2020).
20. Kim, N. D. et al. Chemopreventive and adjuvant therapeutic potential of pomegranate (*Punica granatum*) for human breast cancer. *Breast Cancer Research and Treatment* 71, (3): 203 – 17 (2002).
21. Moga, A. et al. Pharmacological and therapeutic properties of *Punica granatum* phytochemicals: possible roles in breast cancer. *Molecules* **26** (4), 1054 (2021).
22. Fang, L., Wang, H., Zhang, J. & Fang, X. Punicalagin induces ROS-mediated apoptotic cell death through inhibiting STAT3 translocation in lung cancer A549 cells. *J. Biochem. Mol. Toxicol.* **35**, 1–10 (2021).
23. Hun Chang, J. et al. Antitumor activity of pedunculagin, one of the ellagitannin. *Arch. Pharm. Res.* **18**, 396–401 (1995).
24. Das, R. & Woo, J. Identifying the multitarget pharmacological mechanism of action of genistein on lung cancer by integrating network pharmacology and molecular dynamic simulation. *Molecules* **29** (9), 1913 (2024).
25. Liang, J. W. et al. Network pharmacology-based identifcation of potential targets of the flower of *Trollius chinensis* Bunge acting on anti-inflammatory effectss. *Sci. Rep.* **9** (1), 8109 (2019).
26. Barkat, M. A. et al. Bidirectional approach of *Punica granatum* natural compounds: reduction in lung cancer and SARS-CoV-2 propagation. *BMC Complement. Med. Ther.* **25** (1), 32 (2025).
27. Ramarajyam, G., Murugan, R. & Rajendiran, S. Network pharmacology and bioinformatics illuminates punicalagin's pharmacological mechanisms countering drug resistance in hepatocellular carcinoma. *Hum. Gene.* **42**, 201328 (2024).
28. Liu, X. et al. PharmMapper server: A web server for potential drug target identification using pharmacophore mapping approach. *Nucleic Acids Res.* **38**, W609–W614 (2010).
29. Kanehisa, M., Furumichi, M., Sato, Y., Matsuura, Y. & Ishiguro-Watanabe, M. KEGG: biological systems database as a model of the real world. *Nucleic Acids Res.* **53**, D672–D677 (2025).
30. Guo, Q. et al. Current treatments for non-small cell lung cancer. *Front. Oncol.* **12**, 945102 (2022).
31. Abourehab, M. A. S., Alqahtani, A. M., Youssif, B. G. M. & Gouda, A. M. Globally approved EGFR inhibitors: insights into their syntheses, target kinases, biological activities, receptor interactions, and metabolism. *Molecules* **26** (21), 6677 (2021).
32. Bhatu, R., Patil, H. M. & Patel Catalytic Lysine745 targeting strategy in fourth-generation EGFR tyrosine kinase inhibitors to address C797S mutation resistance. *Eur. J. Med. Chem.* **283**, 117140 (2025).
33. Kim, S. et al. PubChem 2025 update. *Nucleic Acids Res.* **53**, D1516–D1525 (2025).
34. Hanwell, M. D. et al. Avogadro: an advanced semantic chemical editor, visualization, and analysis platform. *J. Cheminform.* **4**, 17 (2012).
35. Bateman, A. et al. UniProt: the Universal Protein Knowledgebase in 2025. *Nucleic Acids Res.* **53**, D609–D617 (2025).

36. Gustavsen, J. A., Pai, S., Isserlin, R., Demchak, B. & Pico, A. R. RCy3: Network biology using Cytoscape from within R. *F1000Res* 18, (8):1774 (2019).
37. Oliveros, J. C. Venny. An Interactive Tool for Comparing Lists with Venn's Diagrams. (2024). https://bioinfogp.cnb.csic.es/tools/venny/index.html
38. Szklarczyk, D. et al. STRING v11: protein-protein association networks with increased coverage, supporting functional discovery in genome-wide experimental datasets. *Nucleic Acids Res.* **47** (D1), D607–D613 (2019).
39. Zhou, Y. et al. Metascape provides a biologist-oriented resource for the analysis of systems-level datasets. *Nat. Commun.* **10** (1), 1523 (2019).
40. Berman, H. M. et al. The Protein Data Bank. *Nucleic Acids Res.* **28**, 235–242 (2000).
41. Meng, E. C. et al. UCSF ChimeraX: Tools for structure building and analysis. *Protein Science* **32**, (2023).
42. Morris, G. M. et al. Software news and updates AutoDock4 and AutoDockTools4: Automated docking with selective receptor flexibility. *J. Comput. Chem.* **30**, 2785–2791 (2009).
43. Adasme, M. F. et al. PLIP. : Expanding the scope of the protein-ligand interaction profiler to DNA and RNA. *Nucleic Acids Res* 49, W530–W534 (2021). (2021).
44. Abraham, M. et al. GROMACS Documentation Release 2024 GROMACS Development Team. (2024). 10.5281/zenodo.10589697
45. Huang, J. et al. CHARMM36m: an improved force field for folded and intrinsically disordered proteins. *Nat. Methods*. **14**, 71–73 (2017).
46. Valdés-Tresanco, M. S., Valdés-Tresanco, M. E., Valiente, P. A. & Moreno, E. gmx_MMPBSA: A New Tool to Perform End-State Free Energy Calculations with GROMACS. *J. Chem. Theory Comput.* **17**, 6281–6291 (2021).

Figures

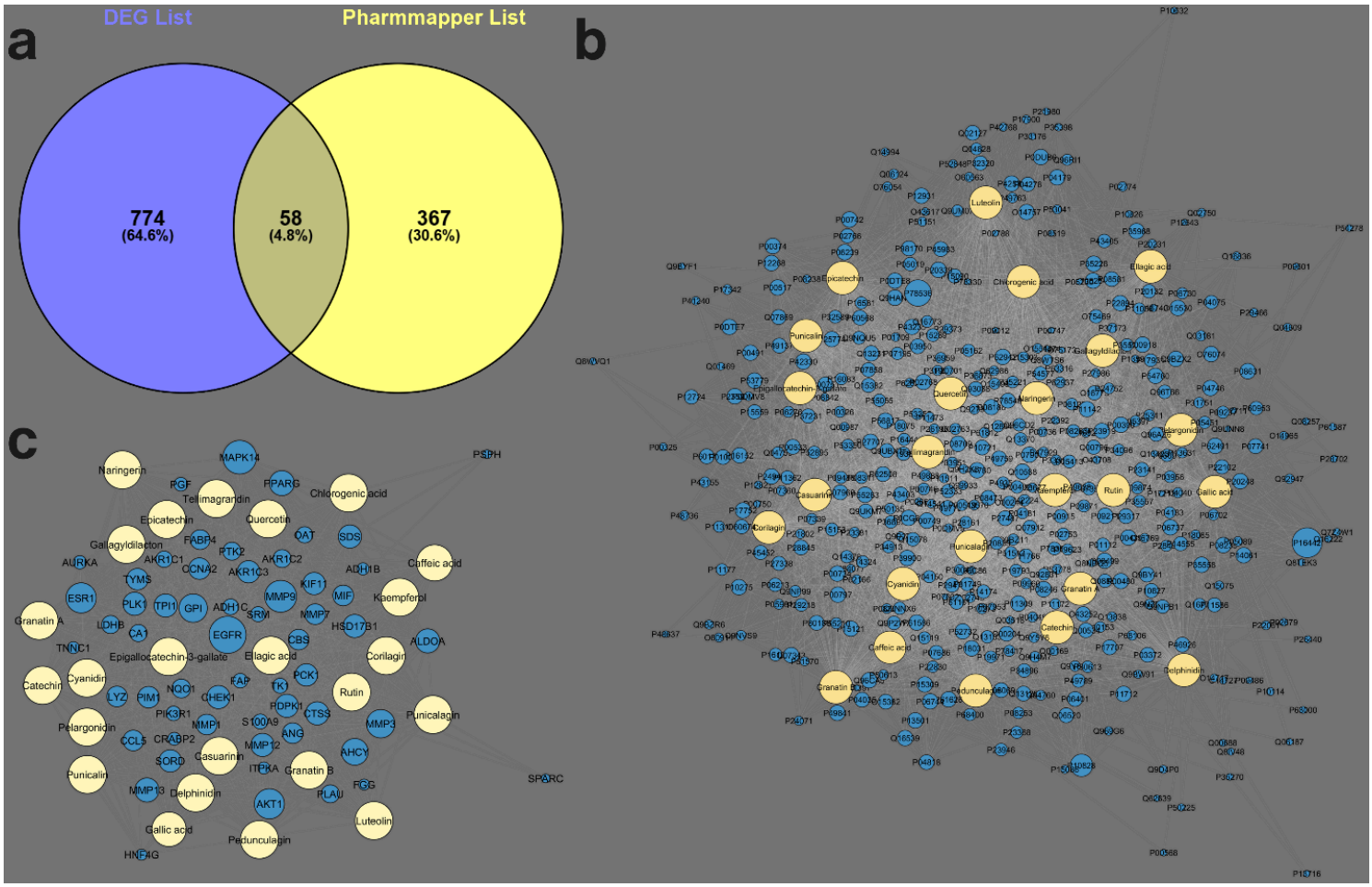


Figure 1

Intersection of *P. granatum* peel compounds and DEGs identified in NSCLC a) Venn diagram of genes found in the accumulated DEG list in relation to the list of potential targets obtained. **b)** The compound-target network of active components of *P. granatum* and their potential proteins targets. Compounds are depicted in yellow, whereas target proteins are depicted in blue. **c)**PPI network of the proteins in overlap list with additional visualization of the compounds' interactions with the target proteins.

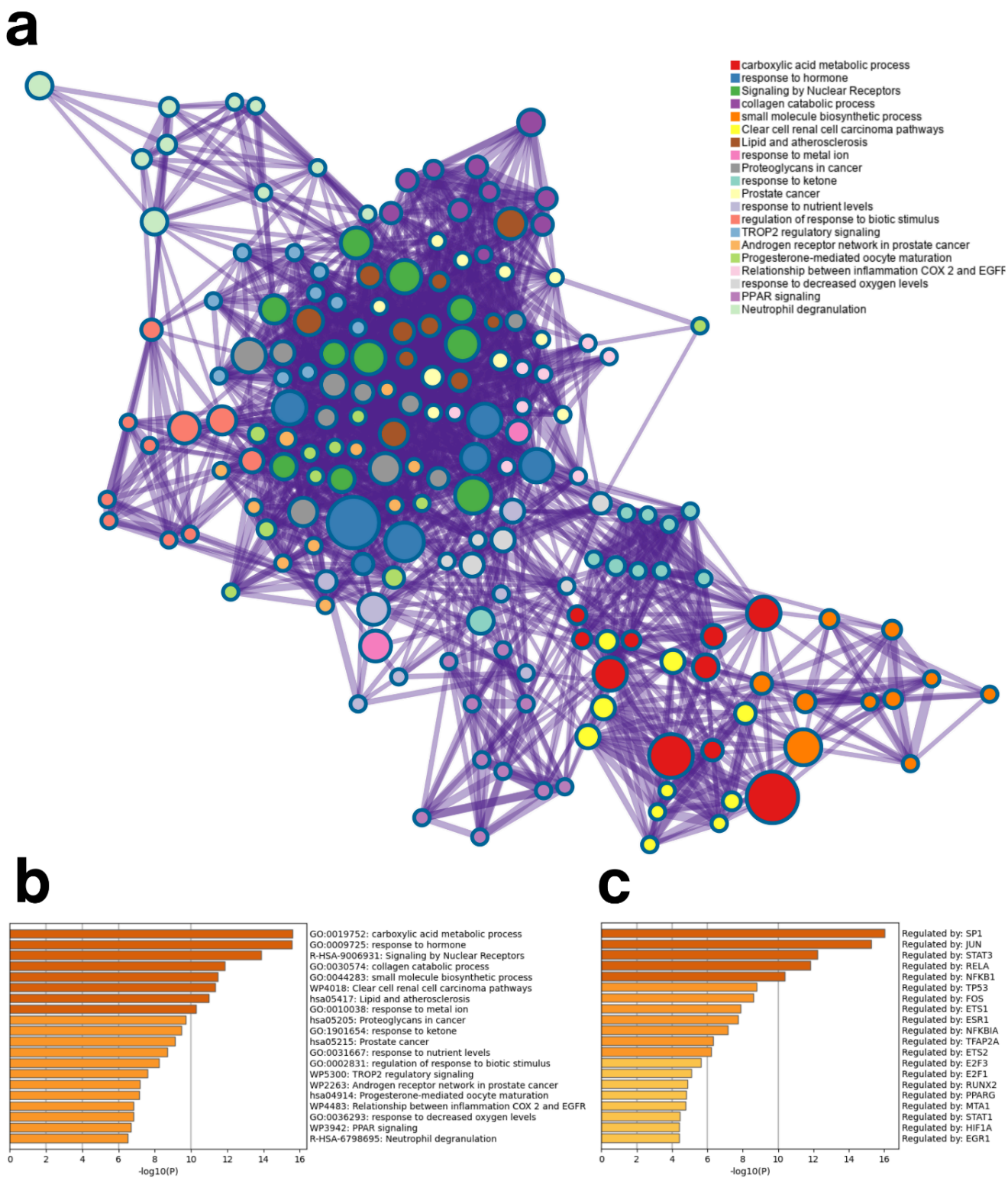


Figure 2

Integrated functional enrichment and pathway analysis of PPI network a) Enrichment network of the overlapping DEGs (different pathways colored differently). **b)** Pathways/biological processes found to be most enriched within the DEG set. **c)**Set of transcription regulators found to most commonly regulate the DEG list. **b** and **c** colored according to p values. **a-c** were produced using Metascape and multiple database data (http://metascape.org/gp/index.html#/main/step1)

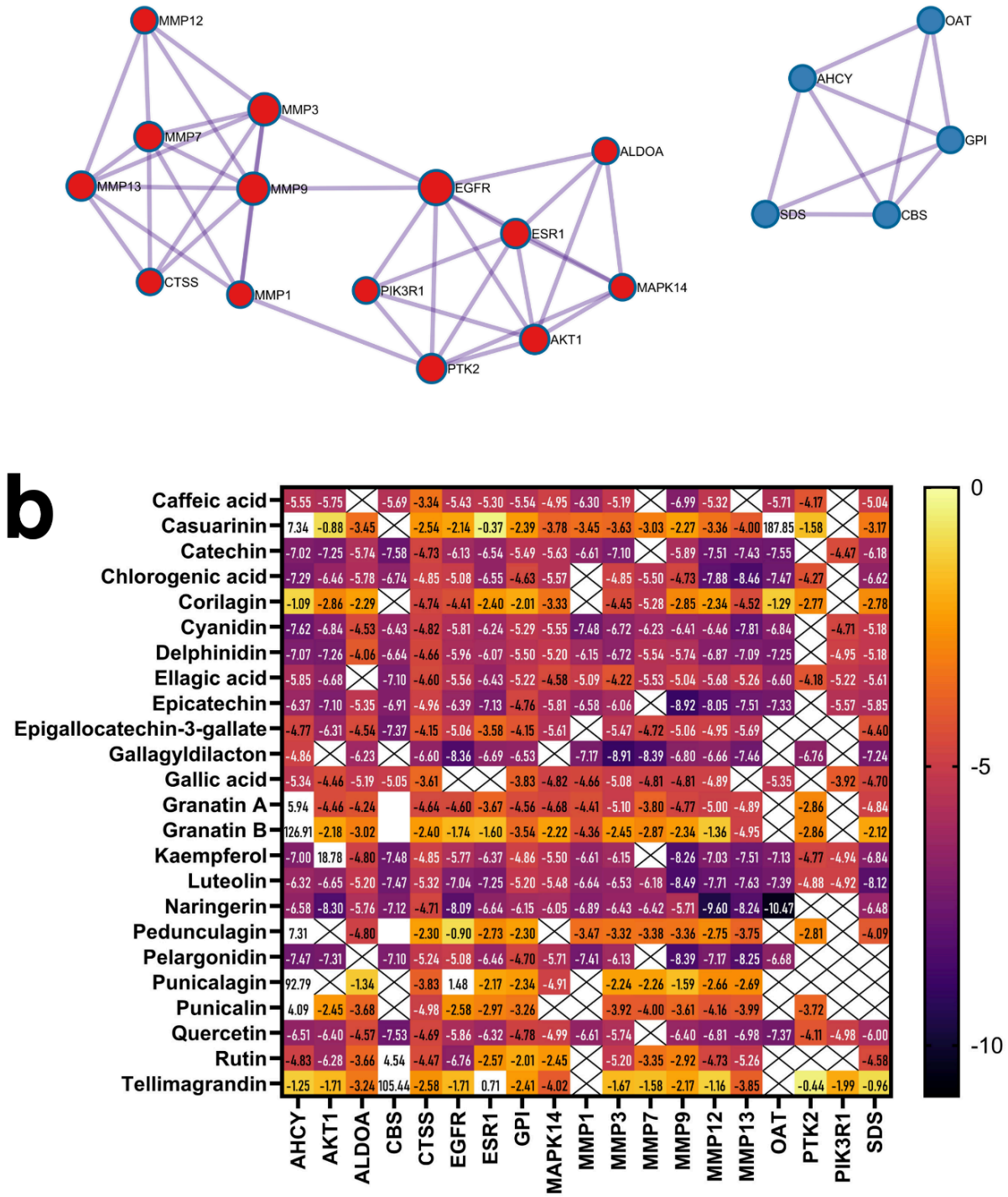


Figure 3

Identification of core target proteins and their potential tendencies towards *P. granatum* peel compounds by docking analysis a) Core target proteins network retracted from the ligand-protein network. The pivotal role of EGFR and its interrelatedness with other members of the core network can be seen. A majority of the members of the secondary core network, represented in blue, have received comparatively recent research attention as the landscape of scientific research shifted interest towards proteins such as PIK3R1 or MAPK14. **b)** Heatmap of all relevant docking permutations which have been executed in this study. Crossed out cells are of those which have not been docked,

while blank cells are of those which produced positive binding energies. The heatmap was created by using GraphPad Prism v.10.6.1.

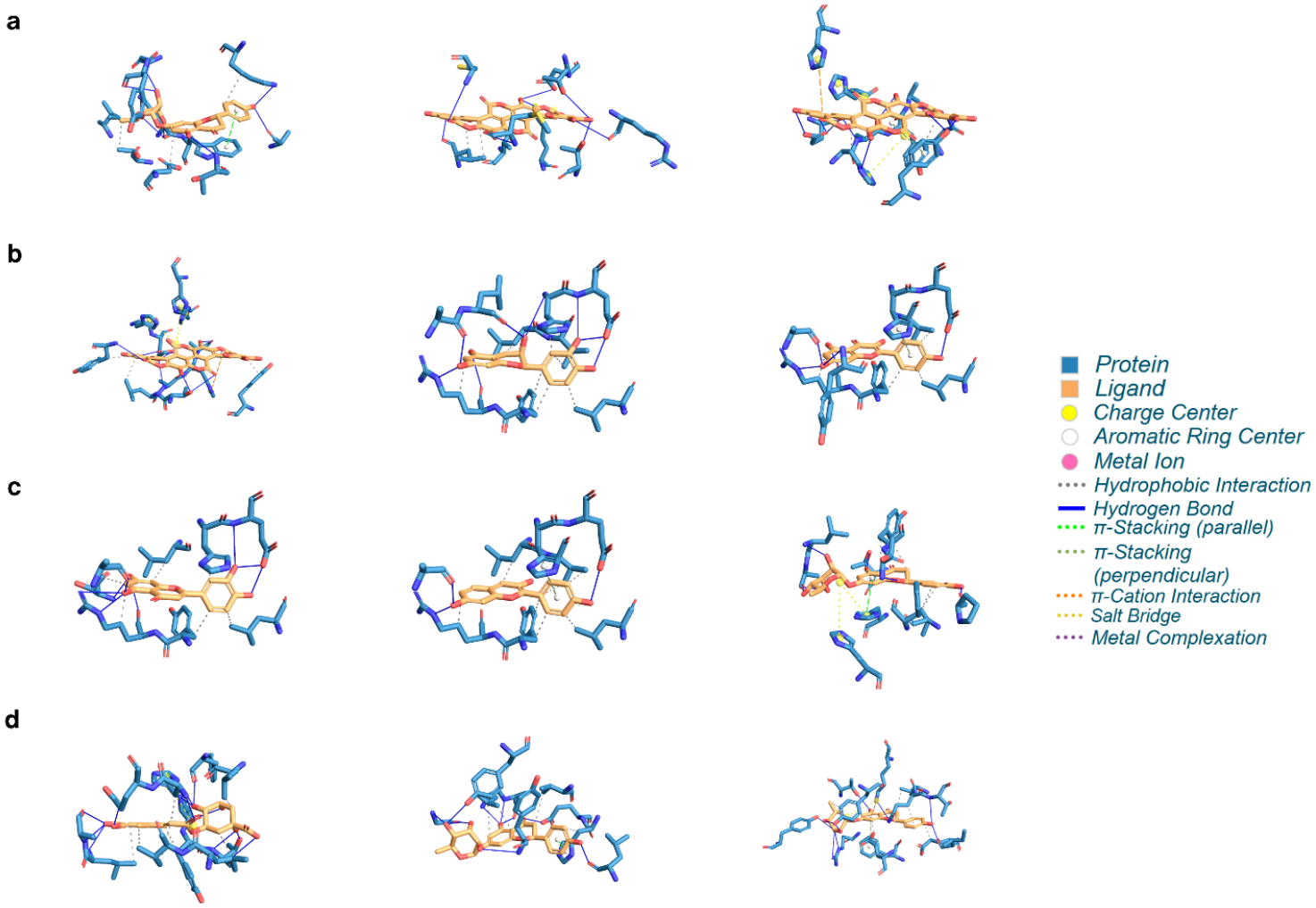


Figure 4

The docking map of compound-target interactions. The 12 complexes computed to be within the nanomolar range can be seen along with the interactions between the proteins and their respective ligands. **a)**(left) AKT1-naringenin, (center) EGFR-gallagyldilacton, (right) MMP3-gallagyldilacton **b)** (left) MMP7-gallagyldilacton, (center) MMP9-epicatechin, (right) MMP9-kaempferol **c)** (left) MMP9-luteolin, (center) MMP9-pelargonidin, (right) MMP12-naringenin **d)** (left) MMP13-naringenin, (center) MMP13-chlorogenic acid, (right) OAT-naringenin.

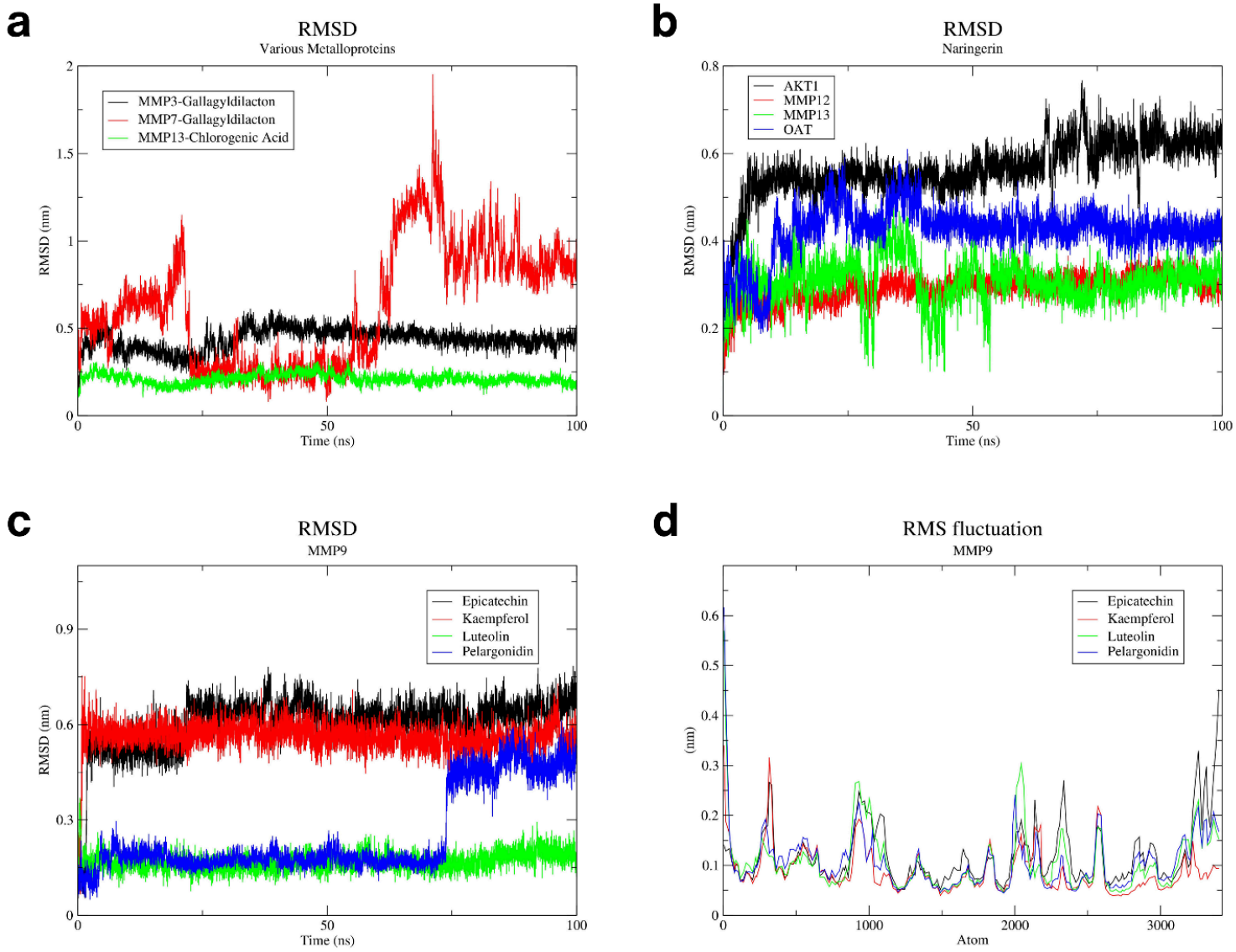


Figure 5

Molecular dynamics simulations of significant compound-target complexes. **a)** RMSD analyses of complexes MMP3-gallagyldilacton, MMP7-gallagydilacton, MMP13-chlorogenic acid. **b)** RMSD analyses of complexes involving naringenin. **c**) MMP9 RMSD results. **d)** RMSF analysis of MMP9 complexes.

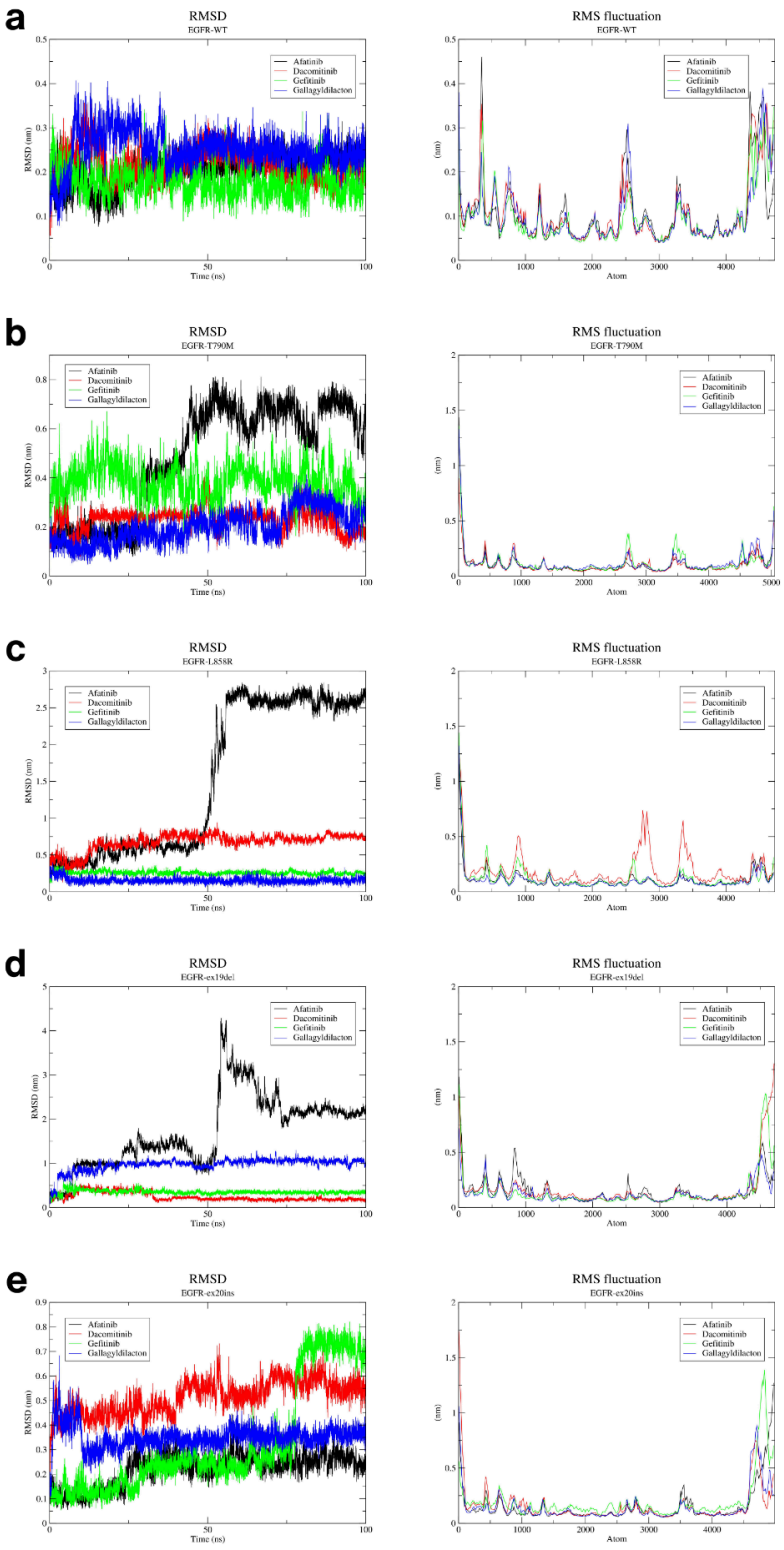


Figure 6

Molecular dynamics simulations of chosen TKIs and gallagyldilacton-EGFR variant protein complexes. RMSD (left column) and RMSF (right column) analysis results of EGFR variants. **a)** $EGFR^{WT}$ **b)** $EGFR^{T790M}$ **c)** $EGFR^{L858R}$ **d)** $EGFR^{ex19del}$ **e)** $EGFR^{ex20ins}$

Supplementary Files

This is a list of supplementary files associated with this preprint. Click to download.

- SupplementaryTables.xlsx
- SupplementaryFigure1RMSDAnalysisofMMP9withvariousligands.png